An efficient 3D finite element procedure for simulating wheel–rail cyclic contact and ratcheting

Ren, Fang; Yang, Zhen; Li, Zili

DOI
10.1016/j.triboint.2024.109878

Publication date
2024

Document Version
Final published version

Published in
Tribology International

Tribology International 198 (2024) 109878

Contents lists available at ScienceDirect

Tribology International

journal homepage: www.elsevier.com/locate/triboint

Full Length Article

An efficient 3D finite element procedure for simulating wheel–rail cyclic contact and ratcheting

Fang Ren, Zhen Yang, Zili Li *

Delft University of Technology, Stevinweg 1, 2628 CN, Delft, The Netherlands

ARTICLE INFO

Keywords:
Ratcheting
Rolling contact fatigue
Finite element
Non-linear kinematic hardening
Contact patch evolution

ABSTRACT

Various models for simulating rail ratcheting behaviour were developed to study rolling contact fatigue (RCF) damage in rails. However, limitations remain in terms of the accuracy of wheel–rail contact modelling and computational efficiency of the cyclic loading simulation. This study developed an efficient 3D finite element (FE) procedure to simulate ratcheting in rails subjected to numerous load cycles. The procedure simulates a wheel rolling repeatedly over a rail section with updated stress–strain states, enabling automatically executed cyclic loading simulation given a predefined number of cycles. To ensure the accuracy of the contact modelling, the effect of meshing schemes on subsurface stress distribution was examined. In addition, the FE contact model with the selected meshing scheme, which balances accuracy and computational efficiency, was verified against the widely accepted CONTACT program. Subsequently, a non-linear kinematic hardening (NLKH) steel material was used in the FE model for ratcheting simulations with up to 100 wheel-loading cycles. The rail surface and subsurface stress states were replicated under partial-slip wheel–rail rolling contact conditions with traction coefficients of 0.10, 0.20 and 0.35, respectively. The ratcheting behaviour was extensively analysed in terms of plastic deformation, contact patch evolution, and ratcheting rates. The simulated plastic deformation was found to alter the contact geometry and thus contact stresses, which in turn affect further accumulation of plastic deformation and subsequent ratcheting strains. These findings highlighted the importance of considering the interplay between the rail ratcheting behaviour of the rail and evolving contact conditions for predicting ratcheting and RCF damage in rails.

1. Introduction

Railway rails suffer from head check (HC), a typical form of RCF that could lead to serious accidents [1]. The direct cause of HC has been attributed to the ratcheting induced by the wheel–rail contact [2–4]. At the wheel–rail contact interface, the significant shear stress caused by friction yields the rail steel and thus generates plastic strain in the rail surface. In the ductile rail surface, ratcheting occurs as plastic strain accumulates with increasing load cycles [5,6]. Cracks initiate when the ratcheting strain or accumulated plastic strain reaches a critical level [7,8].

To effectively simulate the ratcheting behaviour in rails, two key components should be carefully treated in the modelling: material and contact. The material properties of rail steels should be capable of accumulating plastic strains through cyclic loading to exhibit ratcheting behaviour. Material properties have generally been treated either with empirical formulations obtained from twin-disc tests [8,9] or with constitutive models that incorporate NLKH [10–13]. Constitutive models have been increasingly preferred owing to their adaptability across various modelling contexts [14–16], particularly RCF-related FE modelling [17–21].

In terms of the wheel–rail contact modelling, early research largely used (semi-)analytical models to simulate cyclic line contact under prescribed contact stresses [2,18,22–25]. The FE contact modelling has been later introduced, which is capable of handling complex contact scenarios with arbitrary geometries [26–28], non-linear material properties [29–31], and dynamic effects [32–34]. However, FE models are generally computationally demanding for cyclic wheel–rail contact, especially with a large number of loading cycles. Consequently, either simplified 2D [17,31,35] or partial 3D FE contact models (with only a FE rail model under prescribed wheel loads) [36–38], have been employed for ratcheting simulations. The 2D line contact solutions differ from the 3D nature of real-life wheel–rail contact, whereas the approaches with prescribed contact stresses exclude the effect of contact patch evolution [22] with the accumulation of plastic deformation, i.e. the ratcheting, on the contact stresses distribution. 3D FE contact models that comprise both the wheel and rail bodies were recently

* Corresponding author.
E-mail address: Z.Li@tudelft.nl (Z. Li).

https://doi.org/10.1016/j.triboint.2024.109878
Received 18 April 2024; Received in revised form 3 June 2024; Accepted 10 June 2024
Available online 12 June 2024

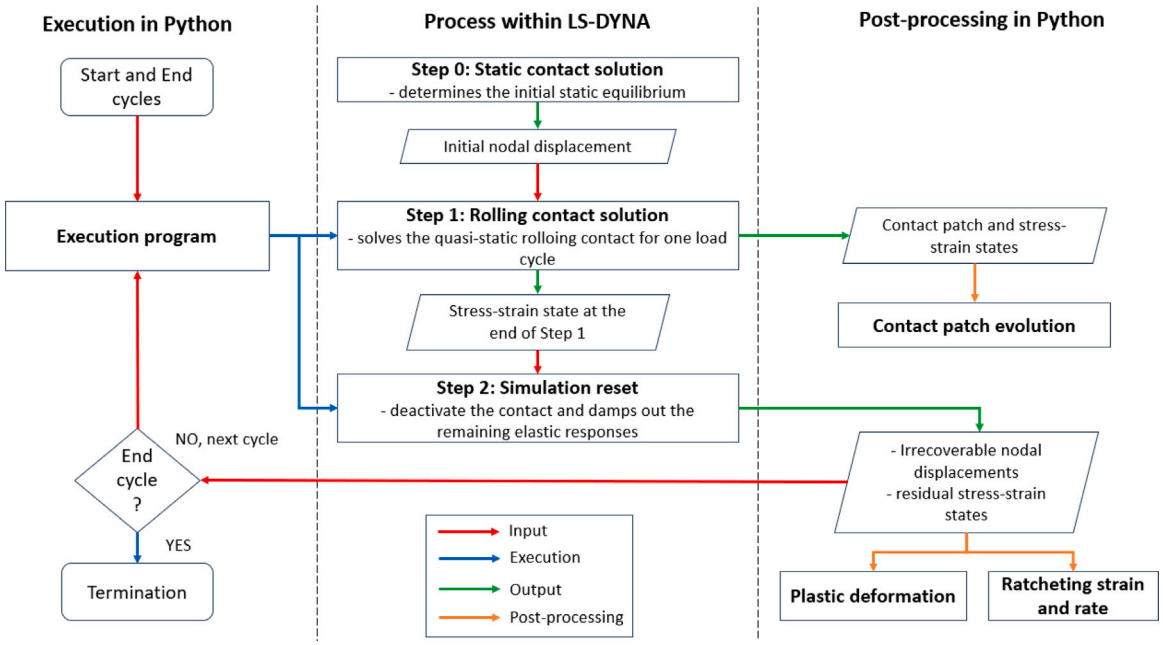

Fig. 1. Automated simulation procedure for cyclic wheel–rail frictional rolling contact loading.

developed for ratcheting simulations [20,39]. These studies highlighted the difference between the contact solutions obtained with 3D contact models and the models mentioned above. However, these studies were either limited by their computation efficiency [39] or primarily focused on the ratcheting of the rail surface from a full-slip contact [20] with less emphasis on different traction conditions and the stress–strain states along the rail depth.

This study introduced a 3D FE contact model, consisting of a complete wheel assembly and a rail section, implemented in an automated procedure for reliably and efficiently simulating wheel–rail cyclic contact loading. The procedure simulated the wheel rolling repeatedly over the rail section with updated contact geometry and stress–strain states. The simulation can be automatically executed for a predefined number of load cycles. The effect of the meshing schemes on the subsurface stress distribution was examined, and the elastic FE contact model with the selected meshing scheme that balances accuracy and computational efficiency was verified against the widely accepted CONTACT programme [40]. Subsequently, the contact solutions for continuous 100 load cycles were reproduced by employing the constitutive material model of R260 rail steel under three loading conditions, corresponding to realistic material and traction conditions tested on the V-Track test rig at TU Delft [41]. The accumulation in plastic deformation and evolutions of the contact patch and stress distribution were then investigated to assess the influence of the traction conditions on the rail ratcheting strains and rates. The next phase of this research will validate the relevant simulation results through physical tests designed to produce HC on V-Track [42].

2. Methodology

This section presents the automated simulation procedure developed to execute simulations for a large number of load cycles. Subsequently, the FE wheel–rail contact model is elaborated. The theoretical background of the NLKH material model and load cases with different traction conditions used in the FE contact model are also explained.

2.1. Simulation procedure

The study developed an automated simulation procedure, shown in Fig. 1, to efficiently simulate cyclic wheel–rail rolling contact. The FE wheel–rail contact modelling was performed using the commercial software package LS-DYNA, and the automated procedure execution and post-processing of the FE solutions were programmed using Python. Each load cycle comprises two steps and takes approximately 25 min (with 16 threads at a 3.7 GHz CPU overclock speed), 3.8 times more efficient than the 3D FE model reported in [39]. This efficiency is notable, considering that the model employs very fine meshes (0.05 mm) at the possible wheel–rail contact region (discussed in Sections 3.1 and 3.2).

As shown in Fig. 1, each load cycle simulation comprises two steps in LS-DYNA (Step 1: Rolling contact simulation, and Step 2: Simulation reset). Before the cyclic loading simulation, the static contact was first solved to obtain the initial equilibrium position of the wheel at Step 0. With the simulation initialised at this static equilibrium position, the simulation duration for the dynamic relaxation, a process for damping out the oscillations caused by the wheel/rail initial kinematic and potential energy from the initial conditions and external loads, can be significantly shortened, enhancing the overall computational efficiency.

The rolling contact simulation can then proceed to Step 1 with a set of traction force and torque applied to achieve the desired traction condition. The FE simulation, with its finely tuned dynamic relaxation settings, can swiftly transition to steady-state rolling contact, which is then maintained to obtain the desired contact patch and stress–strain state (via post-processing with Python), as required for the RCF-related quasi-static analysis [17,20,36,43]. The FE rolling contact simulation resets in Step 2 to prepare for the simulation of the next load cycle. The contact-induced wheel/rail elastic responses obtained in Step 1 are damped out, and the unrecoverable nodal displacements and residual stress–strain states are output. These serve as the initial conditions for the next-cycle rolling contact simulation (if the prescribed number of load cycle numbers has not be reached), and are used for calculating the rail plastic deformation and analysing the rail ratcheting behaviour (via post-processing with Python). The entire procedure for the wheel–rail cyclic loading simulation is automated for an arbitrary number of prescribed load cycles and terminations. It also provides flexibility for adjusting simulation parameters for each cycle, such as loading conditions and wheel speeds.

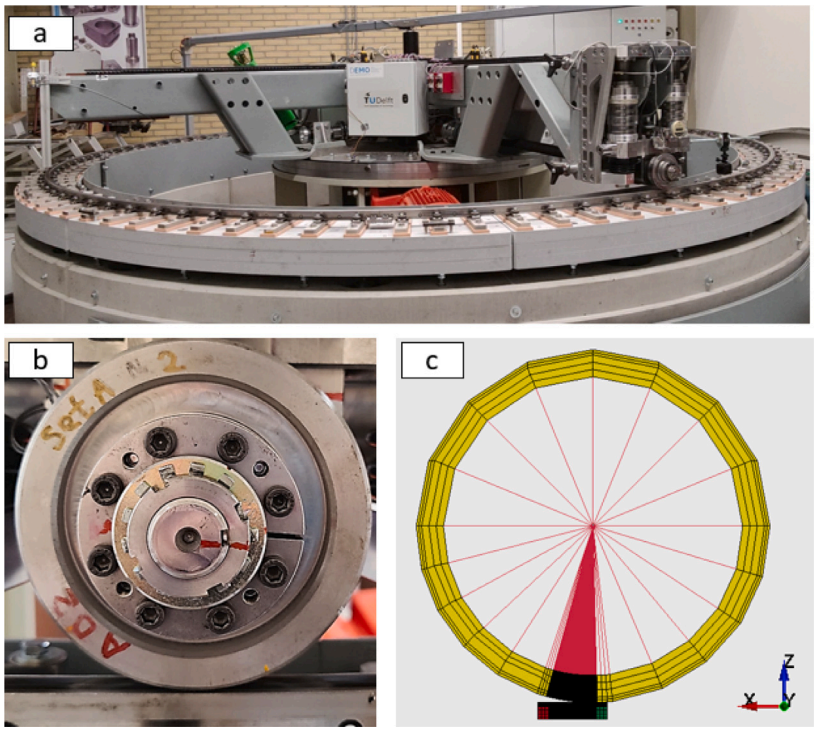

Fig. 2. Test rig and corresponding FE model: (a) overview of the V-Track test rig, (b) close-up of the downscaled wheel and rail, and (c) FE wheel–rail rolling contact model in LS-DYNA.

2.2. Fe model of rail–wheel contact

An FE model was built based on the wheel–rail interaction test rig V-Track [41,44], as shown in Fig. 2. V-Track (Fig. 2(a) and (b)) is developed at TU Delft to study wheel–rail contact and related problems [44–46] including HCs [42]. The contact geometries and loading conditions of the V-Track were replicated using the FE model. The FE model, comprising a wheel and a 20-mm-long rail (Fig. 2(c)), was built using the LS-DYNA software package, widely used for rolling contact simulations [26,47,48]. The calculated FE contact stresses with elastic material were verified using Kalker's CONTACT [40], a boundary-element-based software that has been well acknowledged for solving steady-state rolling contact problems.

To improve the computational efficiency of the FE model, the wheel was simplified to a layer of wheel tread to reduce the number of required element. The wheel tread was connected by rigid beams to a rigid rotating shaft at the centre, as shown in Fig. 3(a). Normal and traction forces, along with the driving torque were applied via the central rotating shaft to the contact interface. The complete circle of the wheel was retained to maintain the balance in inertia during the rolling motion. The rail was reduced to a section of rail head, and the partial model was divided into fine- and coarse-meshed regions on and beneath the rail top surface, as shown in Figs. 3(b) and (c), respectively. The fine mesh zones on the rail top specify the potential contact region to ensure the accuracy of the calculated contact stress and strain [47], as verified in Section 3.2. The fine mesh region was extended to the depth of the rail model, as shown in Fig. 3(c), to precisely evaluate the shear stress and strain distribution in the rail subsurface [9]. This extension is crucial considering that ratcheting develops beneath the rail surface and the subsurface ratcheting strains are often assessed experimentally [8,49]. The distributions of subsurface shear stresses calculated using different meshing schemes are compared and discussed in Section 3.1.

2.3. Material model

This study focussed on the ratcheting behaviour of the rail. Accordingly, the wheel was modelled using elastic material to reduce the computational demand. By contrast, the rail material was represented by a constitutive material model consisting of kinematic and isotropic hardening properties formulated by Chaboche [10,11]. To consider the non-linear effects in kinematic hardening, Chaboche's formulation introduced an evanescent strain memory effect [11] in the change of the deviatoric backstress $d\boldsymbol{\alpha}$, associated with the incremental effective plastic strain, dp as

$$d\boldsymbol{\alpha} = \sum d\boldsymbol{\alpha}_i = \sum \frac{2}{3} C_i d\boldsymbol{\epsilon}_p - \gamma_i \boldsymbol{\alpha}_i dp \tag{1}$$

$$dp = \sqrt{\frac{2}{3}(d\boldsymbol{\epsilon}_p : d\boldsymbol{\epsilon}_p)} \tag{2}$$

where the C_i and γ_i are the plastic modulus and constant, respectively, and $\boldsymbol{\epsilon}_p$ is the plastic strain tensor. The total back stress is the sum of several backstress terms, $d\boldsymbol{\alpha}_i$ that can be specified based on different pairs of C_i and γ_i as shown in Eq. (1).

For isotropic hardening or softening, the change in yield stress, R depends non-linearly on the change in effective plastic strain, dp as follows:

$$dR = b(Q - R)dp \tag{3}$$

where b and Q are isotropic constants that can be determined through cyclic tension–compression tests [50,51]. The yield function incorporates both kinematic and isotropic hardening properties into the von Mises yield criterion $\boldsymbol{\Phi}$ [11,52], as follows:

$$\boldsymbol{\Phi} = \sqrt{\frac{3}{2}(\boldsymbol{s} - \boldsymbol{\alpha}) : (\boldsymbol{s} - \boldsymbol{\alpha})} - (\sigma_{y_0} + R) \tag{4}$$

where $\boldsymbol{s}$ is the deviatoric stress tensor and σ_{y_0} is the initial yield stress.

Table 1 shows the material properties of R260 rail steel [53], used in the FE rail model, considering three pairs of NLKH plastic modulus, C_i and constant γ_i (i= 1, 2, 3). The negative isotropic constant, Q, indicates that the R260 rail softens [53,54] as the effective plastic strain accumulates. Isotropic softening dictates the contraction of the yield surface and tends to affect the ratcheting rate at the early stage [50,55], whereas the kinematic hardening has a more significant influence in later cycles. The ratcheting rate converges when isotropic softening saturates and kinematic hardening stabilises [11,56].

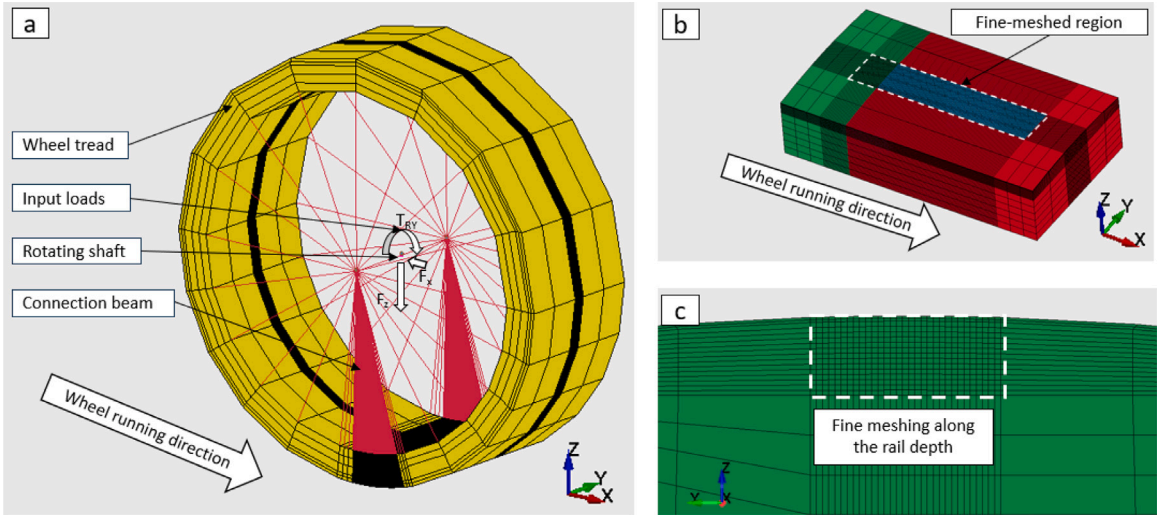

Fig. 3. FE model in LS-DYNA, (a) details of the wheel FE model, (b) the partial rail FE model, and (c) fine meshing along the rail depth.

Table 1
Material properties of R260 rail steel.

Variables	Value	Unit
Q	−189	MPa
b	500	–
C_1	24.7	
C_2	60.0	GPa
C_3	200.0	
γ_1	55	
γ_2	600	–
γ_3	2000	
σ_{y0}	379	MPa
E	206	GPa
υ	0.3	–

Table 2
Simulated load cases and corresponding traction coefficients.

Load case	LC1	LC2	LC3
traction coefficient, μ[−]	0.10	0.20	0.35

2.4. Load cases

Three load cases, LC1, LC2, and LC3, differentiated by the traction coefficient, μ, in Table 2, were simulated to study the influence of traction conditions on rail ratcheting. The traction coefficient is the ratio between the wheel–rail longitudinal and the vertical forces, and is bounded by the friction coefficient. The friction coefficient, f, was set to 0.40 in the study, corresponding to the dry, clean contact condition of the V-Track test rig. For each load case, the vertical force applied to the wheel was 2700 N, generating approximately 1 GPa of maximum wheel–rail contact pressure using the NLKH material.

3. Results

This section first demonstrates the accuracy and validity of the FE wheel–rail contact model by comparing the subsurface shear stress distributions across different meshing schemes and comparing the surface contact stresses calculated using the FE model and CONTACT program. The rail ratcheting behaviour was subsequently analysed in terms of accumulated plastic deformation and contact patch evolution for up to 100 load cycles. The ratcheting strains and rates obtained from the three load cases are compared and discussed.

3.1. Mesh effects and model selection

Four mesh schemes along the depth of the rail model were compared to select an appropriate scheme for the FE ratcheting simulation. The fine-meshed region shown in Fig. 3(c) was further divided into upper and lower parts, demarcated by dashed lines at a normalised depth of 0.1 as shown in Fig. 5. The normalised depth is the depth under the rail surface, z, divided by the semi-axis of the wheel–rail contact area, a (in the X axis defined by the coordinate system in Fig. 3(a), and $a = 1$ mm, as shown in Fig. 5). The FE models using the four mesh schemes were named Model 1 to 4, respectively, as shown in Fig. 5(e). Model 1 had two layers of 0.05 mm-thick elements in the upper part of the fine-meshed region, and the element thickness in the lower part was 1 mm. For Model 2, the 0.05 mm-thickness of the element was kept uniform along the depth. The element thicknesses in the upper and lower parts of Model 3 were 0.025 and 0.1 mm, respectively. The 0.1 mm-thick elements were used in the upper and lower parts of Model 4. Model 4 and 3 had the lowest and highest computational cost.

Figs. 4(a)–(d) compare the subsurface shear stress distributions normalised by the contact pressure ($\tau_{max,ZX}/p_{max}$) in the X–Z plane (coordinate system in Fig. 3 (a)) calculated under four different traction conditions. The stress distribution is presented by the maximum shear stress under the contact patch at different depth positions. Fig. 4(a) shows the case with zero friction force, i.e., traction coefficient μ = 0.00, in which the four models provide similar shear stress distributions along the depth. With an increase of μ, a kink appeared in the shear stress distribution at a normalised depth of 0.05 (except Model 4) and moved downwards, as shown in Fig. 4(b)–(d). Similar patterns in the subsurface shear stress calculations have been reported in [9,27].

Discrepancies among the models appeared in LC1 and LC2 when the kink was located in the upper part of the fine-meshed region (normalised depth $\leq$ 0.1). The kink in the shear stress distribution could not be captured by Model 4 with a coarser mesh, resulting in an underestimation of the shear stress of the surface elements in Model 4, as shown in Figs. 4(b) and (c). Fig. 4(b) indicates that Models 1 and 2 could not fully capture the kink in LC1, however, the calculated shear stresses above and below the kink were well aligned with those of Model 3. Although Model 3 provided the most accurate solutions, its computational cost was two times higher than Model 1 (25 min for one load cycle as reported in Section 2.1) and 1.6 times higher than Model 2. In addition, Model 2, with a finer mesh beneath the normalised depth of 0.1, provided relatively similar results compared with the others. Model 1 was selected for the ratcheting simulations, considering the trade-off between accuracy and computational efficiency.

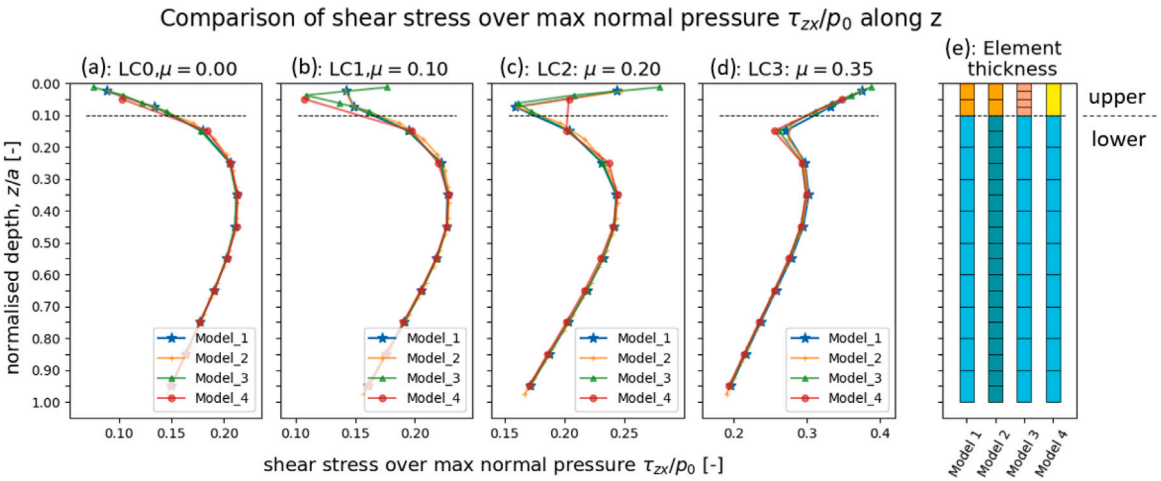

Fig. 4. Normalised subsurface shear stress distributions calculated with different rail mesh densities and traction conditions. (a) traction coefficient $\mu = 0.00$, (b) $\mu = 0.10$, (c) $\mu = 0.20$, (d) $\mu = 0.35$, and (e) subsurface element thicknesses of the four models.

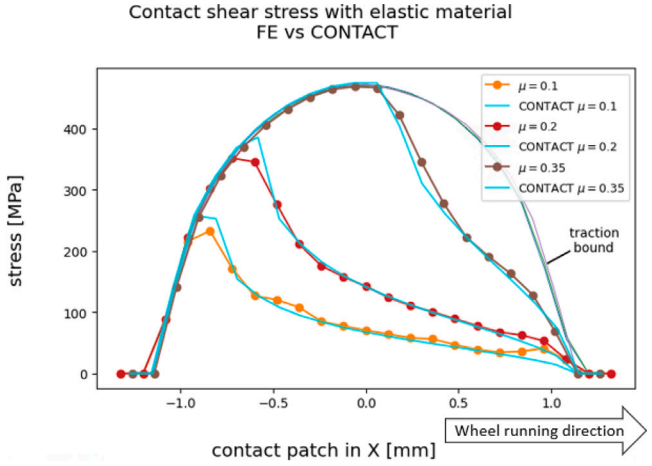

Fig. 5. A comparison of the rail surface shear stresses calculated with FEM and CONTACT under different traction conditions.

3.2. FE model verification

The selected Model 1 was run with the elastic steel material and verified against CONTACT. The wheel–rail surface shear stresses calculated with CONTACT for LC1–LC3 were compared with those calculated with FE Model 1 in Fig. 5. The results indicated good agreement in the distribution and amplitude of the surface shear stresses within the contact patch. Slight deviations were caused by the intrinsic dynamic effects within the FE solutions [47,48].

3.3. Plastic deformation

The verified model was then applied to study the plastic deformation accumulation induced by the wheel–rail contact. Figs. 6–8 show the calculated results for the three load cases, LC1, LC2, and LC3, respectively. The pattern of plastic deformation accumulation is demonstrated by irrecoverable nodal displacements at the rail surface, which can be extracted at every load cycle. In addition to the rail surface nodal displacements after the 1st load cycle, the results from load cycles 5, 35, 60, 75 and 95 are shown in Figs. 6–8, and compared with those calculated after five additional cycles (i.e. from load cycles 10, 40, 65, 80 and 100). Figs. 6–8(a) and (b) show that in both the X–Y and X–Z planes, plastic deformation rapidly accumulated at the early stage (within cycle 10), after which the accumulation rate decreased, eventually stabilising with a minimal increment per cycle. For instance, the plastic deformation accumulation from load cycles 5–10 was less than that in the first five cycles and larger than that from load cycles 35 to 40.

A similar trend, albeit less significant, was observed for plastic deformation in the normal direction of the wheel–rail contact, as presented in the Y–Z plane in Figs. 6–8(c). Figs. 6–8(c) also indicate that the rail surface material was pushed down and outwards owing to the cyclic wheel loading. Consequently, the contact radii of the rail could increase with wheel passage. This could in turn increase the size of the contact patch and reduce contact stresses, slowing the plastic deformation accumulation.

A comparison of the results obtained from the three load cases revealed a significant influence of the traction coefficient, or shear stress, on the wheel–rail contact-induced plastic deformation. The simulated plastic deformation after 100 wheel-loading cycles for LC3 (with $\mu = 0.35$) was approximately 5 times of that for LC2 (with $\mu = 0.20$) and 20 times that for LC1 (with $\mu = 0.10$). The accumulation of plastic deformation slowed rapidly with an increase in load cycle and diminished after approximately 40 cycles when the traction coefficient was 0.10. This confirms that the occurrence of RCF can be effectively prevented by reducing the wheel–rail friction forces.

3.4. Contact patch evolution

The contact-induced plastic deformation in rail head affects the wheel–rail contact solutions. Figs. 9–11 show the evolution of the contact patch and stress states obtained with the NLKH material model (i.e. Model 1 using the NLKH material) based on the results simulated in load cycles 1, 10, 40, 65, 80 and 100, under the three LCs, respectively. Elastic contact solutions are also provided for comparison. Higher amplitudes of the normal and shear surface stresses were obtained when the elastic material was used. In the NLKH case, the distribution of the contact pressure is less symmetrical, with the peak leaning forward, and the width of the contact patch on the X-axis was smaller. These results are consistent with those of previous studies [26,29].

The simulations were able to capture the evolution of the contact patch size at each load cycle. Figs. 9–11 show that the contact patches shrank slightly along the X-axis and expanded significantly along the Y-axis with the load cycles. Contact patch expansion along the Y-axis was expected because the rail head material was pushed outwards due to the cyclic wheel loading, as presented in Figs. 6–8(c), increasing the principal contact radius of the rail. Similar contact patch change patterns were observed in the RCF tests reported in [22]. Similarly, the

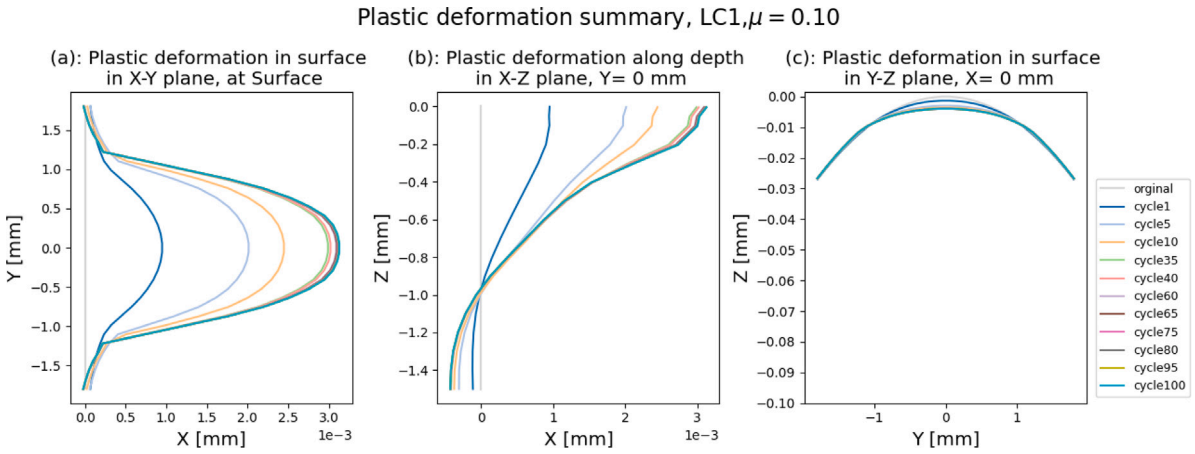

Fig. 6. Accumulation of rail head plastic deformation for LC1 ($\mu = 0.10$): (a) in the X–Y plane, (b): in the X–Z plane, and (c): in the Y–Z plane. N.B. nodal displacement value is not on the same scale in the X and Y axes.

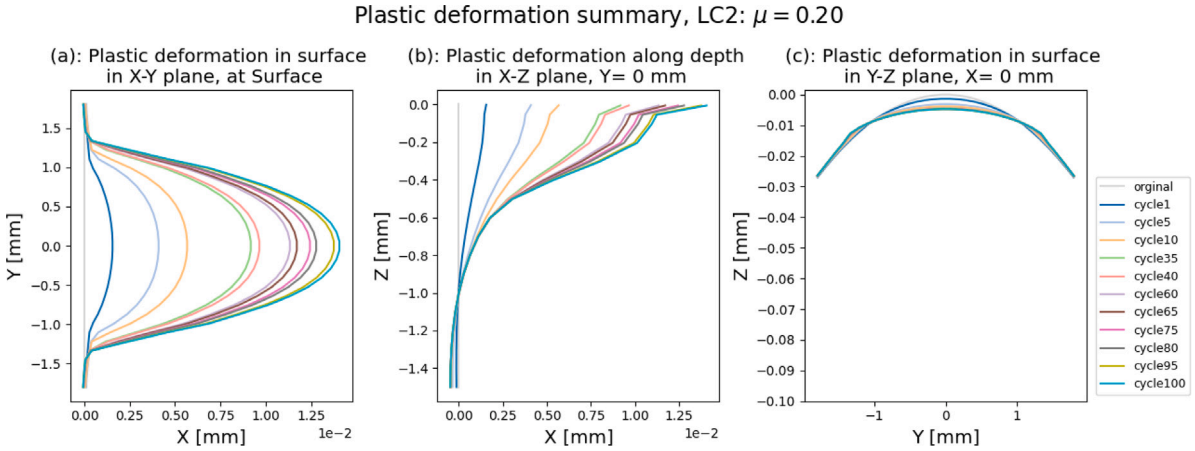

Fig. 7. Accumulation of rail head plastic deformation for LC2 ($\mu = 0.20$): (a) in the X–Y plane, (b): in the X–Z plane, and (c): in the Y–Z plane. N.B. nodal displacement value is not on the same scale in the X and Y axes.

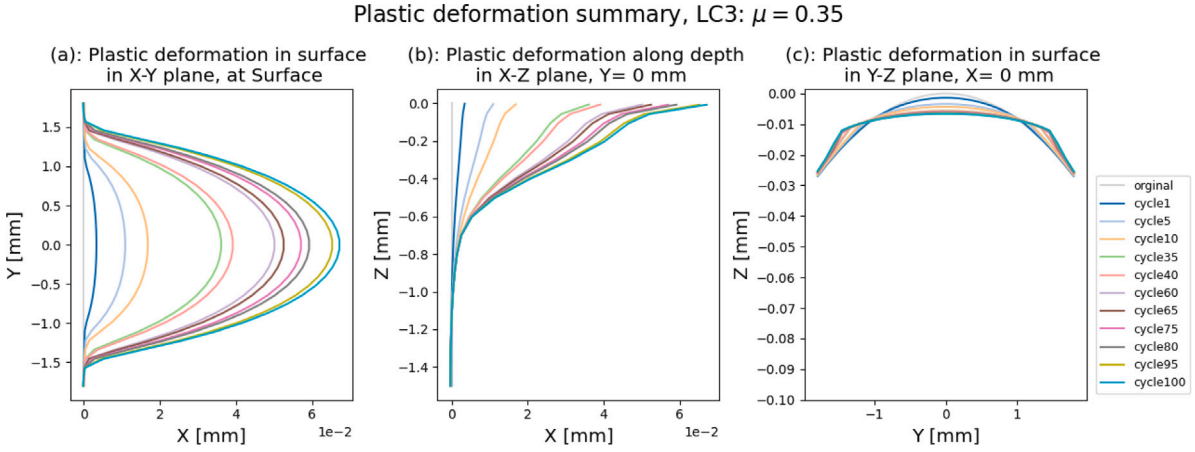

Fig. 8. Accumulation of rail head plastic deformation for LC3 ($\mu = 0.35$): (a) in the X–Y plane, (b): in the X–Z plane, and (c): in the Y–Z plane. N.B. nodal displacement value is not on the same scale in the X and Y axes.

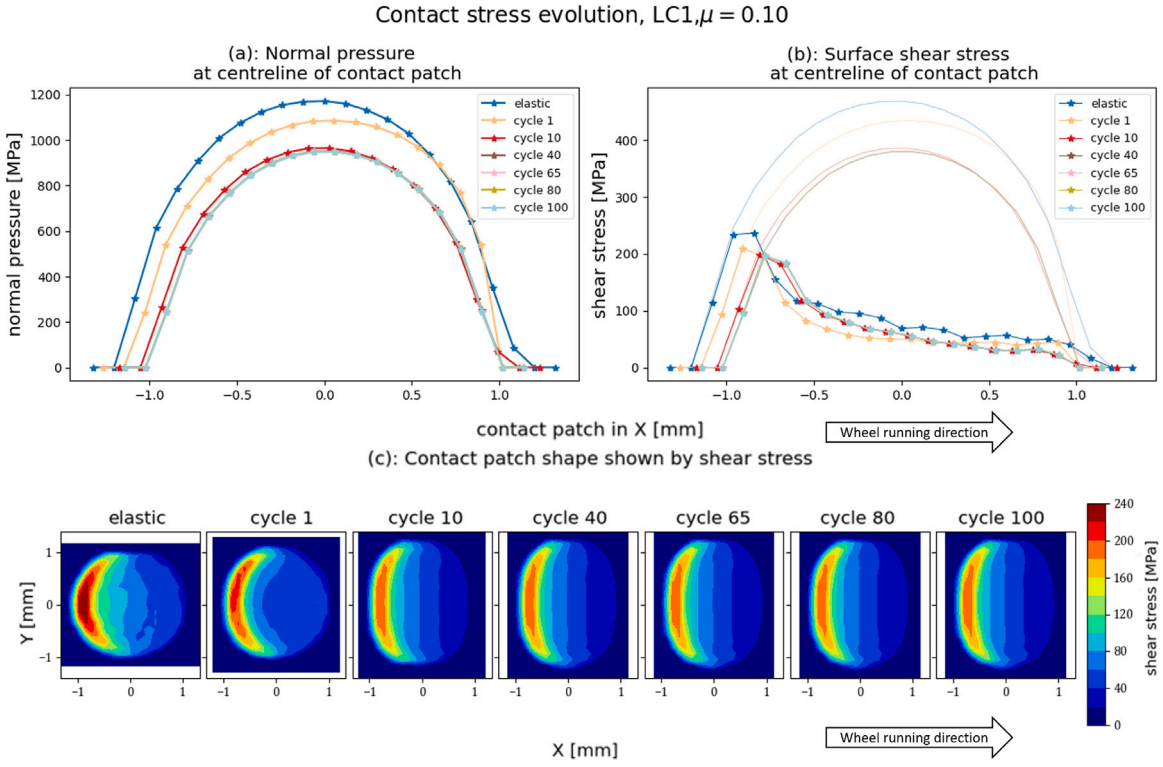

Fig. 9. Evolution of wheel–rail contact stresses for LC1 $\mu = 0.10$: (a) the contact pressure at the centreline of the contact patch, (b) the shear stress at the centre-line of the contact patch, and (c) shear stress within the entire contact patch.

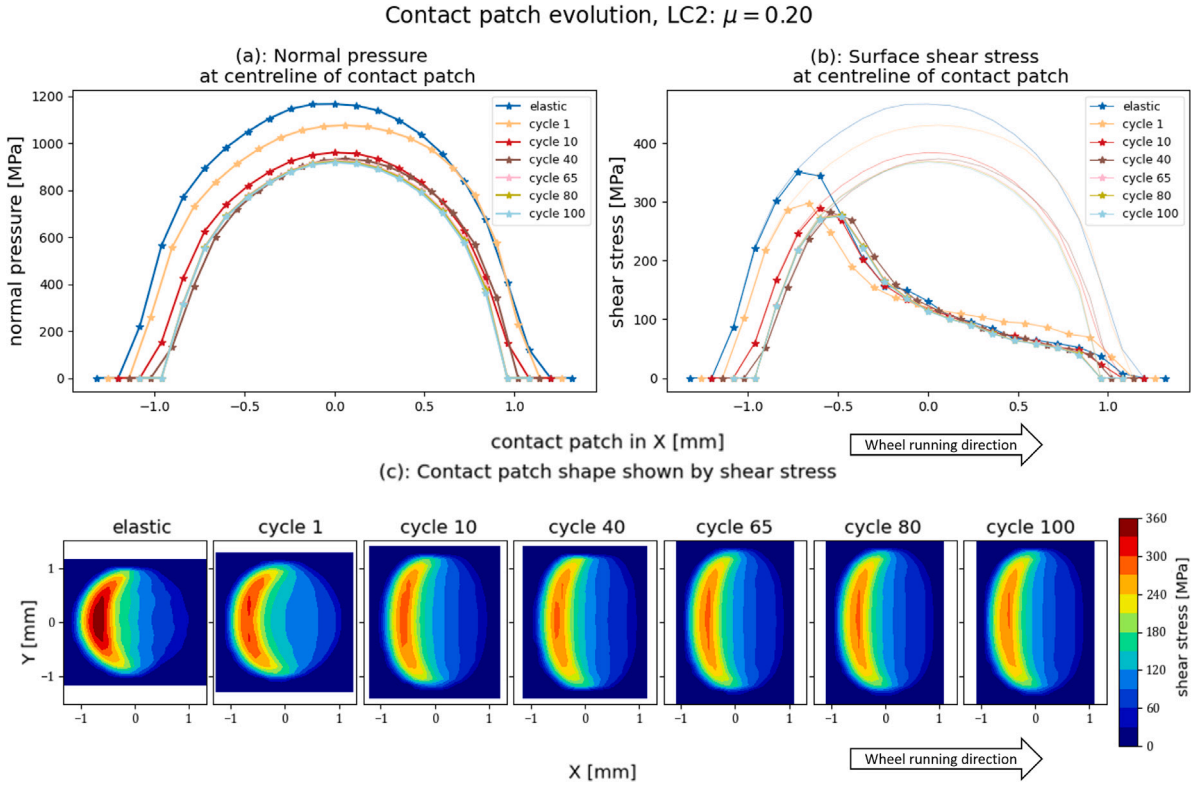

Fig. 10. Evolution of wheel–rail contact stresses for LC1 $\mu = 0.20$: (a) the contact pressure at the centreline of the contact patch, (b) the shear stress at the centre-line of the contact patch, and (c) shear stress within the entire contact patch.

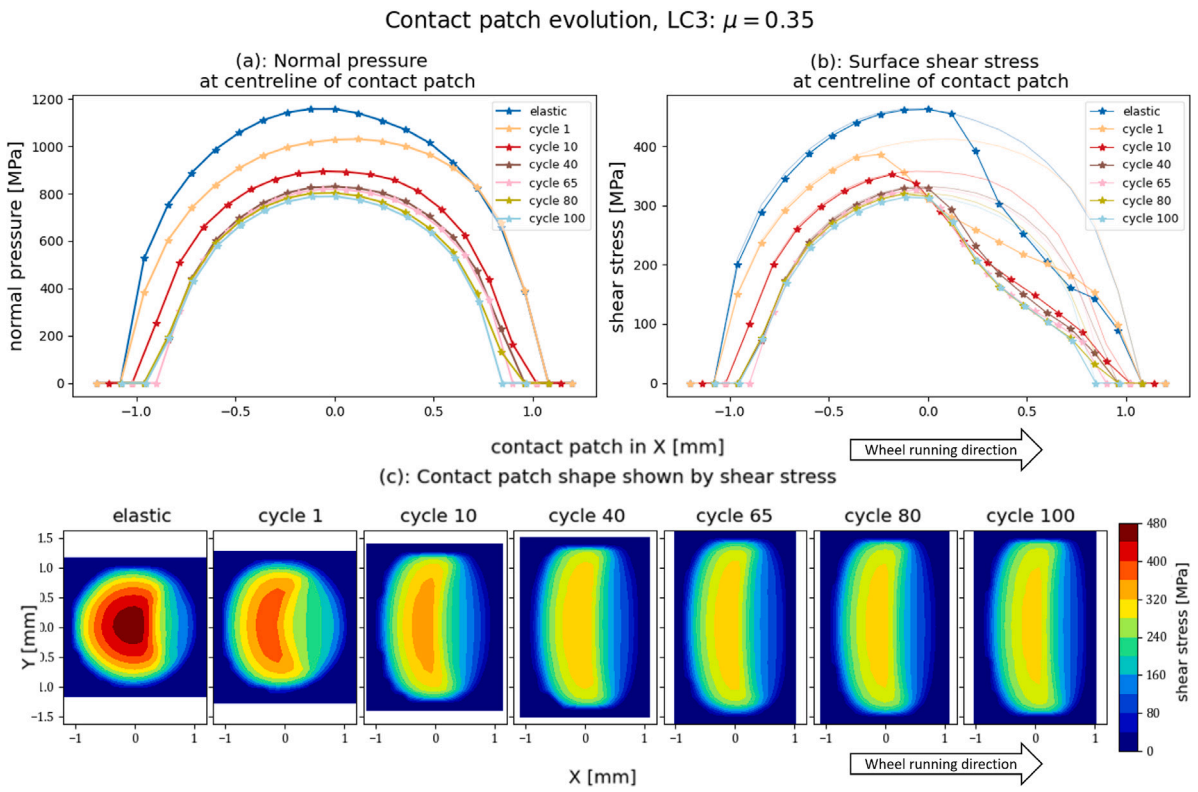

Fig. 11. Evolution of wheel–rail contact stresses for LC1 μ = 0.35: (a) the contact pressure at the centreline of the contact patch, (b) the shear stress at the centre-line of the contact patch, and (c) shear stress within the entire contact patch.

of contact patch evolution was initially rapid and gradually stabilised with increased load cycles.

With the contact patch expansion, the magnitudes of the contact stresses (normal and shear stresses) decreased with increasing load cycles. This pattern was also followed by the stabilisation of the contact stresses after several cycles, corresponding to the change in the contact patch. The decreased contact stresses, in turn, induced less plastic deformation per load cycle until stabilisation was reached. Subsequently, changes in the stresses, plastic deformation, and contact patch size per cycle occurred at a steady but significantly smaller rate. This was observed in Figs. 9–11(c) for the three load cases.

Furthermore, in LC1, the shear stress, size and shape of the contact patch remained nearly unchanged after cycle 40, resembling the shakedown effect [22,57]. By contrast, for the other two cases, a decrease in the contact stresses was observed throughout all 100 cycles. This is because the contact shear stress induced by the low traction force in LC1 could hardly cause the rail material to yield further after 40 cycles. No significant plastic deformation accumulated in the following cycles (presented in Section 3.3) and the ratcheting rate decreased to approximately zero (as shown in Section 3.5). The results align with field observations indicating that HC occurs more frequently on a curved track with higher wheel–rail contact shear stresses [4,58] than on a tangent track.

3.5. Ratcheting rate

This study further analysed the rail ratcheting behaviour by examining the simulated ratcheting strains and rates on the rail surface and beneath the surface at a depth of 150 μm, the same location as concerned in [8]. Because the actual surface ratcheting strains can hardly be measured, subsurface shear strains have often been used to indicate the intensity of ratcheting in rail [8,25,49]. Figs. 12–14 show the results for each load case. Ratcheting was analysed in the ZX shear strains since the longitudinal wheel–rail friction forces predominantly generated contact shear stresses in this study. A common characteristic across the three different load cases was the significant decrease in ratcheting rate with the load cycles at the early stage, followed by stabilisation. Correspondingly, the ratcheting strain rapidly increased at the beginning and then increased linearly with a stabilised ratcheting rate.

The magnitudes of the ratcheting rates for the same number of load cycles differ among the load cases. The simulation case with a higher traction force exhibited a significantly higher ratcheting rate at the initial stage compared with the results in Figs. 12–14(b). For LC1 with the lowest traction force and shear stresses, the converged ratcheting rate was close to zero and no significant increase in the ratcheting strain was observed after cycle 45, as shown in Fig. 12. The rail was effectively in a shakedown state, with no further plastic deformation accumulation [57]. This is also indicated in Fig. 9, where the shear stress remained nearly unchanged after cycle 40. This confirms that the ratcheting behaviour can be substantially limited with a low traction coefficient under the given normal contact force.

Figs. 12–14 also show the differences between the simulated ratcheting strains and rates in the rail surface and those at the subsurface with a depth of 150 μm. Higher ratcheting strains accumulated on the surface after the 100 load cycles. Notably, the gap between the surface and subsurface widened as the traction coefficient increased from 0.10 (LC1) to 0.35 (LC3). The subsurface also yielded lower ratcheting rate under stabilised conditions for LC2 and LC3. By contrast, for LC1, the ratcheting rate at both locations approached zero when the rail reached a shakedown after cycles 40 in the subsurface and 45 in the surface.

A common trend observed in the simulated plastic deformation accumulation and contact patch evolution is their rapid increase within the first few cycles, followed by slowing down and stabilisation, as discussed in Sections 3.3 and 3.4. This trend can be attributed to the

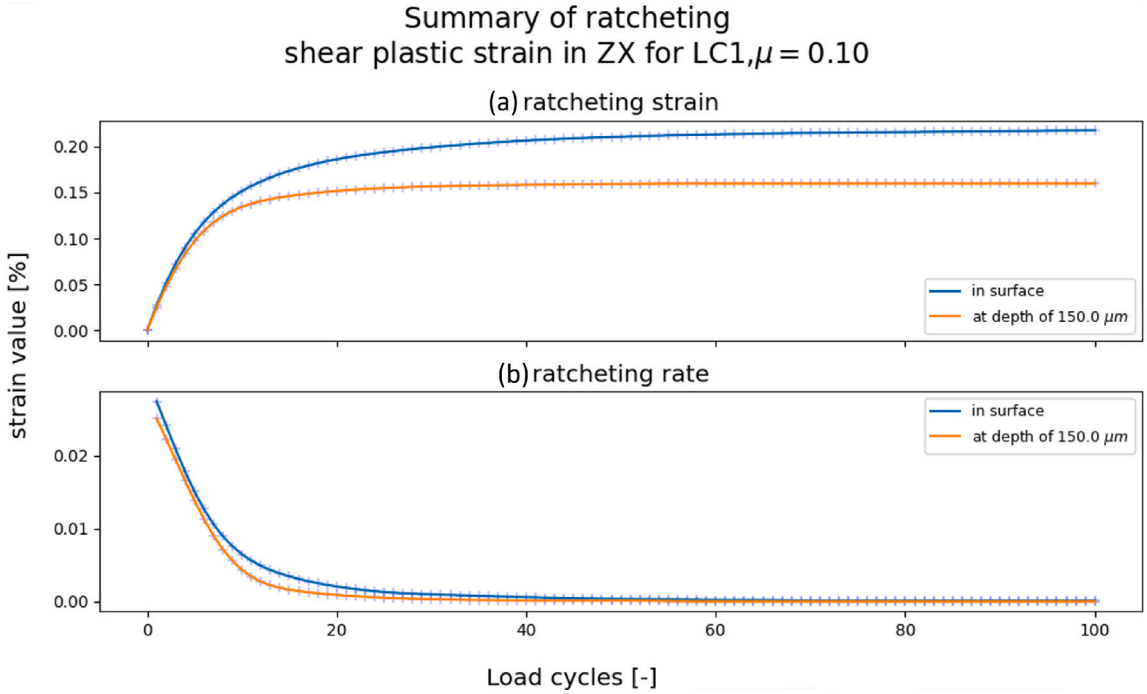

Fig. 12. Ratcheting behaviour on and beneath the rail surface simulated for LC1 ($\mu = 0.10$): (a) ratcheting strain; (b) ratcheting rate.

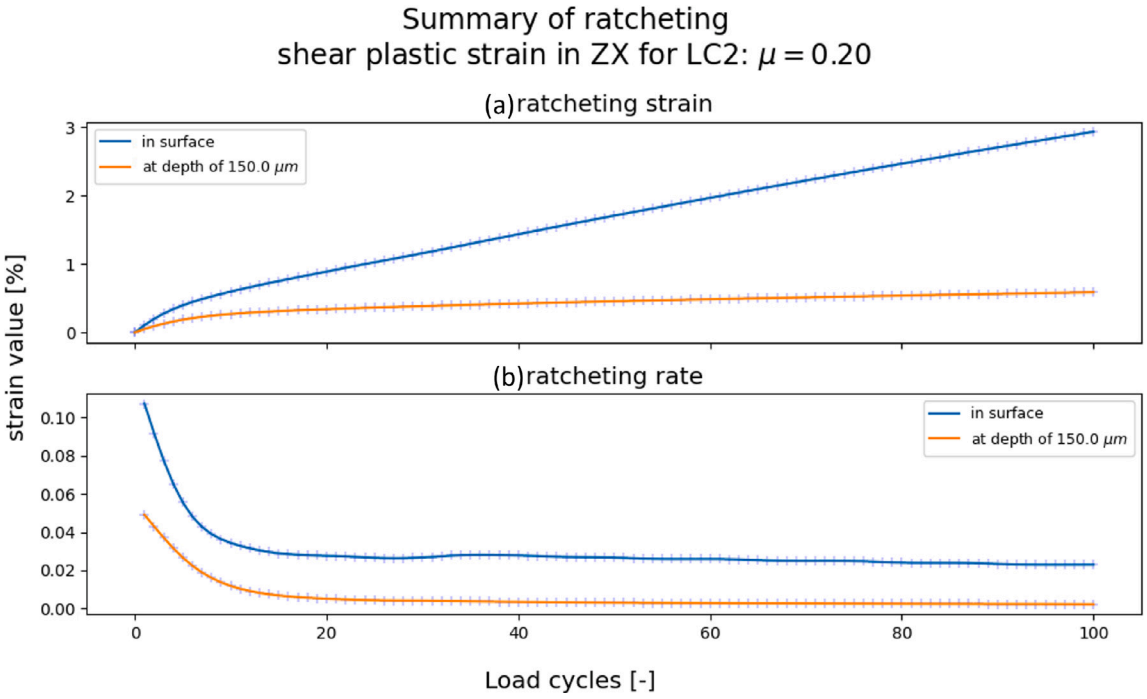

Fig. 13. Ratcheting behaviour on and beneath the rail surface simulated for LC1 ($\mu = 0.20$): (a) ratcheting strain; (b) ratcheting rate.

ratcheting behaviour characterised by the NLKH material applied in this study. In the first few load cycles, the isotropic softening/hardening properties of the material explained in Section 2.3 had more significant influence on the softening process of R260 rail steel with the contraction of yield surface; thus, rapid accumulation of plastic deformation was expected. Isotropic softening tended to saturate with a relatively low effective plastic strain [50], and the kinematic hardening became more dominant in the latter cycles. The small and steady incremental change in the plastic deformation and contact patch can be attributed to the stabilised kinematic hardening.

The ratcheting trend observed in this study is consistent with the findings of previous studies [2,36,59]. However, in contrast to the previous studies suggesting that the ratcheting tends to stabilise within a relatively small number of load cycles in the wheel–rail contact [36, 59], this study indicates that the ratcheting rate may stabilise at a higher number of load cycles. This difference can be attributed to the

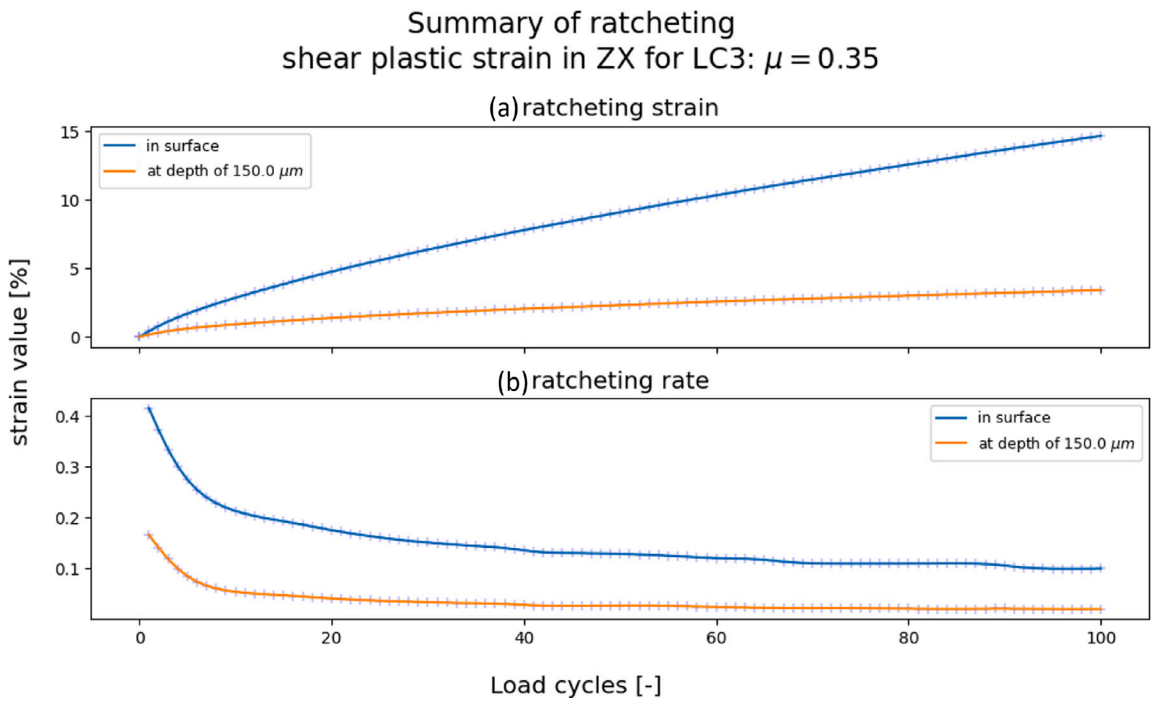

Fig. 14. Ratcheting behaviour on and beneath the rail surface simulated for LC1 ($\mu = 0.35$): (a) ratcheting strain; (b) ratcheting rate.

interplay between the ratcheting behaviour of the rail steel presented by a NLKH material and the evolving contact patches, reproduced in this study but excluded in previous analyses. In particular, for LC3, where the shear stress was high and the contact patch changed significantly, the ratcheting rate shows a declining trend until cycle 80 in Fig. 14(b). This indicates the significance of considering the interplay between ratcheting behaviour and contact patch evolution for accurate rail ratcheting predictions.

4. Conclusions

4.1. Conclusion

This study introduced an efficient 3D FE modelling procedure for simulating rail ratcheting with a large number of wheel-loading cycles. The FE wheel–rail contact model was verified using the CONTACT program, and its meshing scheme was optimised. By applying a NLKH steel material to the FE contact model, the rail ratcheting behaviours with up to 100 partial-slip wheel passages were simulated under different traction conditions. The simulated rail head plastic deformation, wheel–rail contact patch evolution, and ratcheting strains on both the rail surface and subsurface were analysed.

The results revealed that under the cyclic wheel loading the rail surface material was pushed down and outwards and deforms plastically. Consequently, the plastic deformation increased the size of the contact patch, reduced contact stresses, and slowed the plastic deformation. This indicates that the rail plastic deformation accumulation, or ratcheting behaviour, interacted with the contact patch evolution, which expanded in the lateral direction and slightly shrank in the rolling direction. This interplay between the ratcheting behaviour and contact patch evolution should be considered for accurate rail ratcheting and subsequent HC crack initiation predictions.

In addition, the results revealed the accumulation of plastic deformation, evolution of contact patch and increase of ratcheting strain are rapid at the early stage (with a small number of load cycles), and then they become slower with the increase of wheel load cycles and eventually stabilises. Moreover, the study showed that the ratcheting behaviour can be substantially influenced by the traction condition: a larger traction coefficient (0.35) induced substantially higher ratcheting strain and stabilised strain rate, in both the rail surface and subsurface, than a lower traction coefficient (0.10 or 0.20).

4.2. Discussion and further research

The basic Chaboche formulation used in this study to represent the NLKH rail material may have overestimated the plastic strains under multiaxial loading conditions [13,55,60], typically the case for wheel–rail rolling contact. This implies that the ratcheting rate determined in this study may not entirely correspond to the actual HC crack initiation process. A more advanced NLKH material model can be developed and incorporated into the presented modelling procedure to further increase the accuracy of reproducing the rail ratcheting behaviour and subsequent RCF process. Furthermore, the numerical simulation results should be experimentally validated, and tests under loading conditions similar to the simulations presented in this study will be conducted on the V-Track test rig at TU Delft.

In addition, wear, induced by the frictional contact [61], also changes contact profiles during the cyclic wheel–rail rolling contact, and contributes to the evolution of the contact patch in reality. According to the wear calculation method presented in [46], under the contact conditions simulated in this study, the effect of wear on contact solutions was significantly lower than that of ratcheting within the first 100 cycles. However, wear may have substantial effects over a much larger number of load cycles. Therefore, future studies will take into account the influence of wear, especially when addressing a high number of load cycles, to achieve more accurate predictions of contact patch and stress evolution, and ratcheting effects in rails.

CRediT authorship contribution statement

Fang Ren: Writing – original draft. **Zhen Yang:** Writing – review & editing. **Zili Li:** Writing – review & editing.

Declaration of competing interest

There is no conflict of interest.

Data availability

Data will be made available on request.

Acknowledgements

This research is part of the Maximise Rail Life (MaxLife) project, conducted at Delft University of Technology. This project (Code: 15796) was funded by Dutch rail infrastructure manager, ProRail and the Dutch Research Council (NWO).

References

[1] Grassie SL. Rolling contact fatigue on the british railway system: treatment. Wear 2005;258(7–8):1310–8. http://dx.doi.org/10.1016/j.wear.2004.03.065.
[2] Bower A, Johnson K. The influence of strain hardening on cumulative plastic deformation in rolling and sliding line contact. J Mech Phys Solids 1989;37(4):471–93. http://dx.doi.org/10.1016/0022-5096(89)90025-2.
[3] Beynon JH, Garnham JE, Sawley KJ. Rolling contact fatigue of three pearlitic rail steels. Wear 1996;192(1–2):94–111. http://dx.doi.org/10.1016/0043-1648(95)06776-0.
[4] Dollevoet R, Li Z, Arias-Cuevas O. A method for the prediction of head checking initiation location and orientation under operational loading conditions. Proc Inst Mech Eng, Part F: J Rail Rapid Transit 2010;224(5):369–74. http://dx.doi.org/10.1243/09544097jrrt368.
[5] Bower AF. The influence of crack face friction and trapped fluid on surface initiated rolling contact fatigue cracks. J Tribol 1988;110(4):704–11. http://dx.doi.org/10.1115/1.3261717.
[6] Kapoor A. Wear by plastic ratchetting. Wear 1997;212(1):119–30. http://dx.doi.org/10.1016/s0043-1648(97)00083-5.
[7] Kapoor A. A re-evaluation of the life to rupture of ductile metals by cyclic plastic strain. Fatigue Fracture Eng Mater Struct 1994;17(2):201–19. http://dx.doi.org/10.1111/j.1460-2695.1994.tb00801.x.
[8] Tyfour WR, Beynon JH, Kapoor A. Deterioration of rolling contact fatigue life of pearlitic rail steel due to dry-wet rolling-sliding line contact. Wear 1996;197(1–2):255–65. http://dx.doi.org/10.1016/0043-1648(96)06978-5.
[9] Kapoor A, Beynon JH, Fletcher DI, Loo-Morrey M. Computer simulation of strain accumulation and hardening for pearlitic rail steel undergoing repeated contact. J Strain Anal Eng Des 2004;39(4):383–96. http://dx.doi.org/10.1243/0309324041223935.
[10] Frederick CO, Armstrong PJ. A mathematical representation of the multiaxial Bauschinger effect. Mater High Temp 2007;24(1):1–26. http://dx.doi.org/10.3184/096034007x207589.
[11] Chaboche J. Time-independent constitutive theories for cyclic plasticity. Int J Plast 1986;2(2):149–88. http://dx.doi.org/10.1016/0749-6419(86)90010-0.
[12] Chaboche J. On some modifications of kinematic hardening to improve the description of ratchetting effects. Int J Plast 1991;7(7):661–78. http://dx.doi.org/10.1016/0749-6419(91)90050-9.
[13] Ohno N, Wang J. On modelling of kinematic hardening for ratcheting behaviour. Nucl Eng Des 1995;153(2–3):205–12. http://dx.doi.org/10.1016/0029-5493(95)90012-8.
[14] Lu J, Sun W, Becker A, Saad AA. Simulation of the fatigue behaviour of a power plant steel with a damage variable. Int J Mech Sci 2015;100:145–57. http://dx.doi.org/10.1016/j.ijmecsci.2015.06.019.
[15] Xu L, Nie X, Fan J, Tao M, Ding R. Cyclic hardening and softening behavior of the low yield point steel BLY160: Experimental response and constitutive modeling. Int J Plast 2016;78:44–63. http://dx.doi.org/10.1016/j.ijplas.2015.10.009.
[16] Lorenz SJ, Sadeghi F, Wang C. Effect of spatial hardness distribution in rolling contact fatigue performance of bearing contacts. Tribol Int 2022;171:107550. http://dx.doi.org/10.1016/j.triboint.2022.107550.
[17] Ringsberg J. Prediction of fatigue crack initiation for rolling contact fatigue. Int J Fatigue 2000;22(3):205–15. http://dx.doi.org/10.1016/S0142-1123(99)00125-5.
[18] Mazzù A, Petrogalli C, Faccoli M. An integrated model for competitive damage mechanisms assessment in railway wheel steels. Wear 2015;322–323:181–91. http://dx.doi.org/10.1016/j.wear.2014.11.013.
[19] Zhao B, Shen F, Cui Y, Xie Y, Zhou K. Damage analysis for an elastic-plastic body in cylindrical contact with a rigid plane. Tribol Int 2017;115:18–27. http://dx.doi.org/10.1016/j.triboint.2017.05.009.
[20] Pletz M, Meyer KA, Künstner D, Scheriau S, Daves W. Cyclic plastic deformation of rails in rolling/sliding contact –quasistatic FE calculations using different plasticity models. Wear 2019;436–437:202992. http://dx.doi.org/10.1016/j.wear.2019.202992.
[21] Mazzù A, Battini D, Zani N. Computational assessment of ratcheting in rail-wheel contact with solid contaminant. Wear 2024;205346. http://dx.doi.org/10.1016/j.wear.2024.205346.
[22] Kapoor A, Johnson K. Effect of changes in contact geometry on shakedown of surfaces in rolling/sliding contact. Int J Mech Sci 1992;34(3):223–39. http://dx.doi.org/10.1016/0020-7403(92)90073-p.
[23] Johnson KL. Plastic deformation in rolling contact. In: Rolling contact phenomena. Springer Vienna; 2000, p. 163–201. http://dx.doi.org/10.1007/978-3-7091-2782-7_3.
[24] Mazzù A, Donzella G. A model for predicting plastic strain and surface cracks at steady-state wear and ratcheting regime. Wear 2018;400–401:127–36. http://dx.doi.org/10.1016/j.wear.2018.01.002.
[25] Franklin F, Garnham J, Fletcher D, Davis C, Kapoor A. Modelling rail steel microstructure and its effect on crack initiation. Wear 2008;265(9–10):1332–41. http://dx.doi.org/10.1016/j.wear.2008.03.027.
[26] Wei Z, Z. L, Qian Z, Chen R, Dollevoet R. 3D FE modelling and validation of frictional contact with partial slip in compression–shift–rolling evolution. Int J Rail Transp 2015;4(1):20–36. http://dx.doi.org/10.1080/23248378.2015.1094753.
[27] Deng X, Qian Z, Dollevoet R. Lagrangian explicit finite element modeling for spin-rolling contact. J Tribol 2015;137(4). http://dx.doi.org/10.1115/1.4030709.
[28] Yang Z, Li Z, Dollevoet R. Modelling of non-steady-state transition from single-point to two-point rolling contact. Tribol Int 2016;101:152–63. http://dx.doi.org/10.1016/j.triboint.2016.04.023.
[29] Zhao X, Li Z. A three-dimensional finite element solution of frictional wheel–rail rolling contact in elasto-plasticity. Proc Inst Mech Eng, Part J: J Eng Tribol 2014;229(1):86–100. http://dx.doi.org/10.1177/1350650114543717.
[30] Pletz M, Daves W, Yao W, Kubin W, Scheriau S. Multi-scale finite element modeling to describe rolling contact fatigue in a wheel–rail test rig. Tribol Int 2014;80:147–55. http://dx.doi.org/10.1016/j.triboint.2014.07.005.
[31] Daves W, Kubin W, Scheriau S, Pletz M. A finite element model to simulate the physical mechanisms of wear and crack initiation in wheel/rail contact. Wear 2016;366–367:78–83. http://dx.doi.org/10.1016/j.wear.2016.05.027.
[32] Yang Z, Li Z. A numerical study on waves induced by wheel-rail contact. Int J Mech Sci 2019;161–162:105069. http://dx.doi.org/10.1016/j.ijmecsci.2019.105069.
[33] Li S, Naeimi M, He C, Dollevoet R, Li Z. An integrated 3D dynamic FE vehicle-track model in elasto-plasticity to investigate short pitch corrugation under cyclic wheel loads. Structures 2023;53:1000–11. http://dx.doi.org/10.1016/j.istruc.2023.05.001.
[34] Wu B, Wang W, Pan J, Hu Y, Xu R, Ye D, et al. Study on corrugated wear on high-speed railways based on an improved finite element model of wheel-rail rolling contact. Tribol Int 2023;179:108199. http://dx.doi.org/10.1016/j.triboint.2022.108199.
[35] Chen H, Ji Y, Zhang C, Liu W, Chen H, Yang Z, et al. Understanding cementite dissolution in pearlitic steels subjected to rolling-sliding contact loading: A combined experimental and theoretical study. Acta Mater 2017;141:193–205. http://dx.doi.org/10.1016/j.actamat.2017.09.017.
[36] Pun CL, Kan Q, Mutton PJ, Kang G, Yan W. An efficient computational approach to evaluate the ratcheting performance of rail steels under cyclic rolling contact in service. Int J Mech Sci 2015;101–102:214–26. http://dx.doi.org/10.1016/j.ijmecsci.2015.08.008.
[37] Zhou Y, Zheng X, Jiang J, Kuang D. Modeling of rail head checks by X-ray computed tomography scan technology. Int J Fatigue 2017;100:21–31. http://dx.doi.org/10.1016/j.ijfatigue.2017.03.005.
[38] Li Y, Wu Y, Mutton P, Qiu C, Yan W. A ratcheting mechanism-based numerical model to predict damage initiation in twin-disc tests of premium rail steels. Eng Fail Anal 2023;146:107066. http://dx.doi.org/10.1016/j.engfailanal.2023.107066.
[39] Zhou Z, Li W, Wen Z, Zhou S, Tao G. Three-dimensional elastic–plastic stress analysis of wheel–rail cyclic rolling contact using finite element method. Wear 2024;542–543:205277. http://dx.doi.org/10.1016/j.wear.2024.205277.
[40] Kalker JJ. Three-dimensional elastic bodies in rolling contact. Netherlands: Springer; 1990, URL https://www.ebook.de/de/product/2225648/j_j_kalker_three_dimensional_elastic_bodies_in_rolling_contact.html.
[41] Naeimi M, Li Z, Petrov RH, Sietsma J, Dollevoet R. Development of a new down-scale setup for wheel-rail contact experiments under impact loading conditions. Exp Tech 2017;42(1):1–17. http://dx.doi.org/10.1007/s40799-017-0216-z.
[42] Ren F, Yang Z, Hajizad O, Moraal J, Li Z. Experimental investigation into the initiation of head check damage using V-Track. In: 12th international conference on contact mechanics and wear of rail/wheel systems, 4-7 September 2022, Melbourne, Victoria, Australia. 2022.
[43] Popov VL. Contact mechanics and friction. Berlin, Heidelberg: Springer; 2010, p. 301–22. http://dx.doi.org/10.1007/978-3-642-10803-7.
[44] Zhang P, Moraal J, Li Z. Design, calibration and validation of a wheel-rail contact force measurement system in V-Track. Measurement 2021;175:109105. http://dx.doi.org/10.1016/j.measurement.2021.109105.
[45] Yang Z, Zhang P, Moraal J, Li Z. An experimental study on the effects of friction modifiers on wheel–rail dynamic interactions with various angles of attack. Railw. Eng. Sci. 2022;30(3):360–82. http://dx.doi.org/10.1007/s40534-022-00285-y.
[46] He C, Yang Z, Zhang P, Li S, Naeimi M, Dollevoet R, et al. A finite element thermomechanical analysis of the development of wheel polygonal wear. Tribol Int 2024;195:109577. http://dx.doi.org/10.1016/j.triboint.2024.109577.
[47] Zhao X, Li Z. The solution of frictional wheel–rail rolling contact with a 3D transient finite element model: Validation and error analysis. Wear 2011;271(1–2):444–52. http://dx.doi.org/10.1016/j.wear.2010.10.007.

[48] Yang Z, Deng X, Li Z. Numerical modeling of dynamic frictional rolling contact with an explicit finite element method. Tribol Int 2019;129:214–31. http://dx.doi.org/10.1016/j.triboint.2018.08.028.

[49] Kapoor A, Franklin FJ. Tribological layers and the wear of ductile materials. Wear 2000;245(1–2):204–15. http://dx.doi.org/10.1016/S0043-1648(00)00480-4.

[50] Karvan P, Varvani-Farahani A. Isotropic-kinematic hardening framework to assess ratcheting response of steel samples undergoing asymmetric loading cycles. Fatigue Fract Eng Mater Struct 2018;42(1):295–306. http://dx.doi.org/10.1111/ffe.12905.

[51] Nath A, Ray KK, Barai SV. Evaluation of ratcheting behaviour in cyclically stable steels through use of a combined kinematic-isotropic hardening rule and a genetic algorithm optimization technique. Int J Mech Sci 2019;152:138–50. http://dx.doi.org/10.1016/j.ijmecsci.2018.12.047.

[52] Mises Rv. Mechanik der festen körper im plastisch- deformablen zustand. Nachrichten von der Gesellschaft der Wissenschaften zu Göttingen, Math-Physikalische Klasse 1913;1913:582–92, URL http://eudml.org/doc/58894.

[53] Schleinzer G, Fischer F. Residual stresses in new rails. Mater Sci Eng A 2000;288(2):280–3. http://dx.doi.org/10.1016/s0921-5093(00)00872-8.

[54] Pun CL, Kan Q, Mutton PJ, Kang G, Yan W. Ratcheting behaviour of high strength rail steels under bi-axial compression–torsion loadings: Experiment and simulation. Int J Fatigue 2014;66:138–54. http://dx.doi.org/10.1016/j.ijfatigue.2014.03.021.

[55] Chen X. On the ohno-wang kinematic hardening rules for multiaxial ratcheting modeling of medium carbon steel. Int J Plast 2005;21(1):161–84. http://dx.doi.org/10.1016/j.ijplas.2004.05.005.

[56] Bari S, Hassan T. An advancement in cyclic plasticity modeling for multiaxial ratcheting simulation. Int J Plast 2002;18(7):873–94. http://dx.doi.org/10.1016/s0749-6419(01)00012-2.

[57] Bower A, Johnson K. Plastic flow and shakedown of the rail surface in repeated wheel-rail contact. Wear 1991;144(1–2):1–18. http://dx.doi.org/10.1016/0043-1648(91)90003-d.

[58] Dollevoet R. Design of an anti head check profile based on stress relief (Ph.D. thesis), 2010, p. 151. http://dx.doi.org/10.3990/1.9789036530736.

[59] Su H, Pun CL, Mutton P, Kan Q, Yan W. Numerical study on the ratcheting performance of heavy haul rails in curved tracks. Wear 2019;436–437:203026. http://dx.doi.org/10.1016/j.wear.2019.203026.

[60] Bari S, Hassan T. Anatomy of coupled constitutive models for ratcheting simulation. Int J Plast 2000;16(3–4):381–409. http://dx.doi.org/10.1016/s0749-6419(99)00059-5.

[61] Andersson S. Friction and wear simulation of the wheel–rail interface. In: Lewis R, Olofsson U, editors. Wheel–rail interface handbook. Elsevier; 2009, p. 93–124. http://dx.doi.org/10.1533/9781845696788.1.94.